Multiphysics analysis of cryogenically cooled photocathode in a continuous wave SRF injector cavity

Dmitry Bazyl,* Klaus Floettmann, Elmar Vogel, and Igor Zagorodnov
Deutsches Elektronen-Synchrotron DESY, Notkestrasse 85, 22607, Hamburg, Germany

(Received 15 August 2025; accepted 12 December 2025; published 20 January 2026)

The paper evaluates the thermal regime of a cryogenically cooled copper photocathode integrated into a continuous-wave superconducting radio-frequency injector cavity with direct thermal contact. Such a photoinjector layout is being developed at DESY and has recently demonstrated a record-high 50 MV/m axial electric field in radio-frequency tests, marking an important milestone. To address the thermal effect of the picosecond excitation laser, we first develop a two-temperature model to describe the temperature of the emitting surface at cryogenic temperatures and solve it numerically. Subsequently, we present a one-temperature model of the bulk photocathode coupled with an electromagnetic model of the injector cavity. For the current injector design, we predict a negligible impact of the laser on the intrinsic quality factor of the cavity, identifying instead the cryogenic stability of the copper cathode as the primary operational limit. To overcome cooling challenges, we propose an improved configuration of the cathode plug. For the proposed geometry, the multiphysics analysis confirms stable performance at a nominal 2 W laser power, sufficient for 100 pC beams at 1 MHz under optimistic quantum efficiency assumptions. Operation at higher laser loads will benefit from further dedicated cryogenic analysis.

DOI: 10.1103/9jyv-hfxy

I. INTRODUCTION

A superconducting radio-frequency (SRF) photoinjector is being developed at DESY, aiming to enable high-duty-cycle/continuous wave (cw) operation in a future upgrade of the European X-ray Free-Electron Laser [1,2]. The core feature of the DESY cw SRF injector design is a photocathode insertion method [3]. The cathode is thread mounted to the backside of the SRF injector cavity made of superconducting niobium. This design has experimentally demonstrated an axial electric field up to 50 MV/m in radio-frequency vertical tests [4]. The result supports the fundamental feasibility of generating 100 pC electron bunch charge with a transverse slice emittance below 0.2 μm [5]. Such a photocathode insertion method omits complexities associated with load-lock systems and, overall, this type of injector serves as a promising candidate to fulfill many demanding scientific applications beyond electron sources for cw linacs driving FELs, such as cw ultrafast electron diffraction [6] and cw THz radiation [7] sources. A unique feature of this photoinjector is the direct 2 K cooling interface of the photocathode via superfluid helium.

A limited number of studies address the characteristics of copper photocathodes at cryogenic temperatures. Most available data concern photoemissive properties of copper such as quantum efficiency (QE) and mean transverse energy (MTE). One study showed that the QE of polycrystalline Cu decreases by a factor of 4 when the substrate temperature is lowered from 400 to 85 K [8]. Tests at the bERLinPro injector demonstrated a QE of 10^{-5} at 257 nm with a Cu insert at 80 K [9]. The record low-emittance benchmark for Cu(100) with 5 meV MTE at 35 K was reported in [10].

In the context of photoinjector systems operating in the cryogenic range, thermal stability of the SRF cryogenic assembly of the injector cavity and the photocathode is a necessary prerequisite for stable operation. Previous research on the SRF injector thermal management has mostly focused on systems incorporating load-lock mechanisms for photocathode insertion. For such systems, thermal simulations and measurements have been performed to study the heat generated on a retractable cathode stalk, which acts as the primary heat leak and requires intermediate cooling stages (e.g., 77 K intercepts or active gas cooling) as reported in [11]. For the same injector type with a load-lock system, the finite element method (FEM) has been implemented to carry out thermal studies [12]. Closer to our direct cathode mount configuration, Schultheiss *et al.* [13] studied the thermal behavior of an

*Contact author: dmitry.bazyl@desy.de

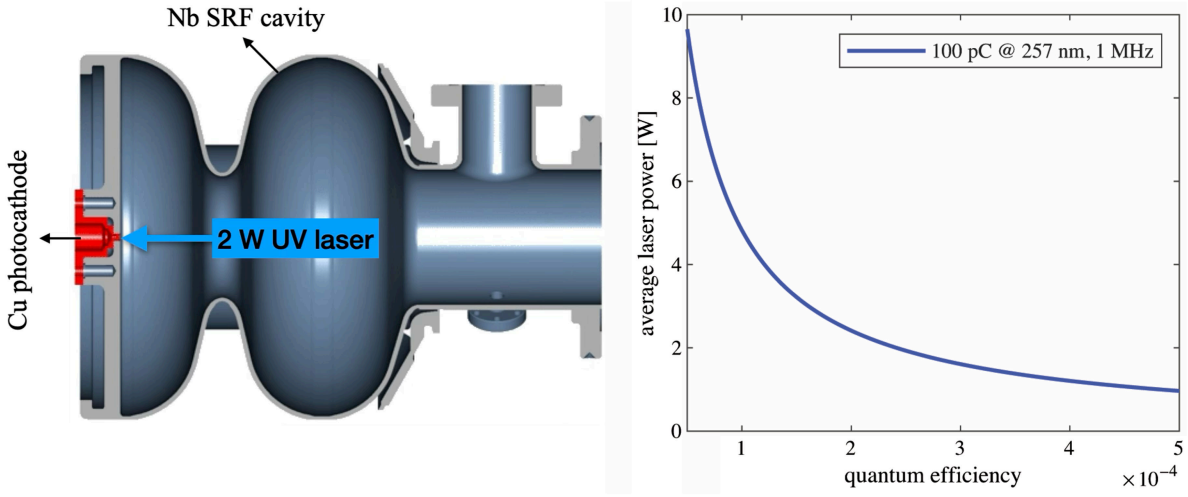

FIG. 1. Image on the left shows the three-dimensional layout of the cw SRF injector cavity with an integrated copper photocathode. The plot on the right presents the average laser power required for a Cu photocathode as a function of QE, assuming a 1 MHz repetition rate and 100 pC bunch charge (257 nm excitation laser).

SRF injector cavity operated at 4.2 K, made of residual-resistance ratio (RRR) 300 niobium, where the photocathode is part of the cavity's backside. The injector cavity under rf load and 1 W laser heating was analyzed, and it was shown that the injector cavity temperatures remained below the superconducting critical temperature. The application of FEMs for thermal modeling at cryogenic temperatures is robust with results often matching experimentally obtained data [14,15].

The cw SRF photoinjector with backside thread mounting of the cathode (see Fig. 1) assumes that most of the heat transfer from the Cu cathode to the superconducting Nb cavity occurs indirectly via an indium sealing. The dissipated rf power in the SRF cavity P_{d} is directly proportional to the surface resistance of the conducting material. The surface resistance $R_s(T)$ of superconducting niobium is a combination of the residual resistance and the temperature-dependent Bardeen–Cooper–Schrieffer (BCS) resistance [16]. The dissipated power is related to the total surface resistance and the quality factor as follows [17]

$$P_{\mathrm{d}}(T) = \frac{1}{2}\int_S R_s(T)|\mathbf{H}_t|^2 dS, \qquad Q_0 = \frac{\omega U}{P_{\mathrm{d}}}, \tag{1}$$

where $|\mathbf{H}_t|$ is the magnitude of the tangential magnetic field at the surface S, ω is the angular resonant frequency, and U is the energy stored in the cavity.

For FEL applications, we consider a design case in which a Cu photocathode must deliver 100 pC electron bunches at repetition rates up to 1 MHz. Under a very demanding QE specification of $(1-2.5)\times 10^{-4}$ at 257 nm, this corresponds to an average UV laser power in the range of approximately 2–5 W, as illustrated in the right plot of Fig. 1. For comparison, the rf power dissipated over the backside of the SRF injector cavity is around 1 W at an axial field of 50 MV/m. Therefore, a substantial laser power deposited into the cryogenic system must be addressed to confirm the thermal stability as well as the absence of a quality factor degradation due to potentially increased rf losses.

The considered QE range should be understood as target specifications constrained by the available and foreseeable UV laser power (e.g., PHAROS systems providing about 2 W at 257 nm [18]), rather than a proven performance of Cu photocathode at cryogenic temperatures in cw operation. Available experimental data indicate that quantum efficiencies at the level of $\sim 10^{-4}$ for polycrystalline copper in normal-conducting S-band rf guns at room temperature are rare and should be regarded as exceptional. Qian *et al.* [19] reported $\mathrm{QE} \simeq 1.5\times 10^{-4}$ at an accelerating field of about 50 MV/m, while Noakes *et al.* [20] observed initial $\mathrm{QE} = (2-3)\times 10^{-4}$ from BPS172-treated hybrid Mo/Cu photocathodes in the CLARA 10 Hz gun, with comparatively limited $1/e$ lifetimes of order 10–60 days. The STFC experience provides a practical motivation to adopt the BPS172 chemical preparation procedure for the photocathode in the present SRF injector design.

The problem of the thermal stability of a cw SRF injector cavity with a Cu cathode integrated via a thread-mounted connection is unique and therefore has not been previously addressed in the literature. To our knowledge, no prior work has solved a two-temperature model for copper initialized in the cryogenic regime under UV excitation. To address these questions, we have developed the required models and used COMSOL Multiphysics® v6.3 [21] to analyze the complex thermal problem of the cold cathode integrated into the SRF injector cavity.

The analysis reveals a potential cryogenic instability in the baseline cathode plug geometry [22], leading us to

propose and evaluate a modified design for enhanced thermal stability at a nominal incident laser power of 2 W.

We start in Sec. II by developing a two-temperature model to describe the temperature of the emitting surface at cryogenic temperatures and solve it numerically to characterize the surface temperature evolution of the cryogenically cooled Cu photocathode during picosecond ultraviolet (UV) laser irradiation and to obtain the time-dependent heat flux for the macroscopic model. In Sec. III, we analyze the two-dimensional transient thermal behavior of the bulk cathode and assess the validity of steady-state thermal analysis in regions distant from the effective emission surface (the Cu-Nb contact interface). Finally, in Sec. IV, we evaluate a coupled three-dimensional thermal-electromagnetic model where the influence of heat induced by the photocathode laser on the dissipated rf power is studied.

II. ONE-DIMENSIONAL TRANSIENT THERMAL ANALYSIS OF A PHOTOEMISSIVE SURFACE

In order to capture the ultrafast thermal dynamics in a copper photocathode at cryogenic temperatures during and after laser irradiation, we employ a one-dimensional two-temperature model (TTM). It resolves the electron temperature T_e and lattice temperature T_l as a function of depth x from the irradiated surface [23] and reads

$$C_e(T_e)\frac{\partial T_e}{\partial t}=\frac{\partial}{\partial x}\left[K_e(T_e,T_l)\frac{\partial T_e}{\partial x}\right]-G(T_e,T_l)(T_e-T_l)+S_{\text{laser}}(x,t), \tag{2}$$

$$C_l(T_l)\frac{\partial T_l}{\partial t}=\frac{\partial}{\partial x}\left[K_l(T_l)\frac{\partial T_l}{\partial x}\right]+G(T_e,T_l)(T_e-T_l), \tag{3}$$

where C_e and C_l are the volumetric heat capacities of the electron and lattice subsystems, respectively; K_e and K_l are the corresponding thermal conductivities; G is the electron-phonon coupling factor that quantifies the volumetric rate of energy exchange between the two subsystems; and S_{laser} is the volumetric laser heat source term.

The domain spans $x\in[0,L_x]$ with $L_x=50$ μm. The relatively large simulation domain (compared to typical conditions for TTM models at room temperatures) is motivated by the exceptionally low heat capacity and high thermal conductivity of cryogenic copper, which leads to a rapid heat transport. Sensitivity tests with $L_x=70$ μm and $L_x=100$ μm confirmed that the near-surface temperature evolution remains unchanged. Thus, we ensure that the ultrafast near-surface electron and lattice temperature dynamics, which govern the net electron-phonon energy exchange, are not prematurely influenced by the thermal conditions imposed at the rear boundary. The initial conditions are given by $T_e(x,0)=T_l(x,0)=T_0$ ($T_0=2$ K). A zero-flux boundary condition is applied at $x=0$, while Dirichlet boundary condition $T_e=T_l=T_0$ is imposed at $x=L_x$.

A two-temperature model for a copper photocathode under ultrashort laser pulse excitation has previously been considered for room-temperature copper in [24]. To validate our numerical model, we successfully reproduced selected results.

In the following subsections, we extend this model to our case of interest at cryogenic temperatures. We have conducted a review of the available literature to combine theoretical and experimental results in order to obtain the required coefficients at cryogenic temperatures for the 1D-TTM. The obtained equations are solved numerically for a representative laser-source configuration defined by the use-case scenario. The results are then applied in Sec. III in the one-temperature modeling of the injector.

A. Properties of copper at cryogenic temperatures

In the following subsections, we provide analytical definitions of the material properties of copper required to solve the 1D-TTM in the cryogenic temperature range. The lattice thermal conductivity $K_l(T_l)$ is omitted due to its negligible contribution for high-purity copper across the entire temperature range and the fact that $K_e\gg K_l$ [25].

1. Electron-phonon coupling factor G

The electron-phonon coupling factor $G(T_e,T_l)$ quantifies the volumetric rate of energy exchange between the electron and lattice subsystems. While G is often treated as a constant in room-temperature TTM, its strong temperature dependence requires an accurate description of the thermal dynamics, which starts from the cryogenic regime. At very low temperatures (significantly lower than the Debye temperature, $T\ll\Theta_D$), the energy transfer rate per unit volume, P_{ep}/V, between electrons at T_e and a lattice at T_l in clean, three-dimensional metals is theoretically predicted to follow a power law [26–28]. Specifically, for energy transfer limited by electron interactions with 3D acoustic phonons, this rate is given by

$$P_{ep}/V=\Sigma_0(T_e^5-T_l^5), \tag{4}$$

where Σ_0 is a material-specific coupling coefficient. The T^5 dependence arises from the temperature dependence of both the available phonon states and the electron phase space for scattering [29]. The electron-phonon coupling factor $G(T_e,T_l)$ is defined such that $P_{ep}/V=G(T_e,T_l)(T_e-T_l)$. Thus, from Eq. (4), the low-temperature form of G is

$$G_{\text{low}}(T_e,T_l)=\Sigma_0\sum_{k=0}^{4}T_e^{4-k}T_l^k. \tag{5}$$

For copper, the material coefficient $\Sigma_0=2.1\times10^9$ W m^{-3} K^{-5} is adopted. This value is supported by

direct experimental measurements on copper thin films that exhibit 3D phonon behavior at sub-Kelvin temperatures [30] and is also consistent with earlier work on similar metallic systems [28]. For instance, if $T_e = T_l = T$, then $G_{\mathrm{low}}(T,T) = 5\Sigma_0 T^4$. At $T = 2$ K, this yields $G_{\mathrm{low}} \approx 1.68 \times 10^{11}$ W m^{-3} K^{-1}, and at $T = 27$ K, $G_{\mathrm{low}} \approx 5.58 \times 10^{15}$ W m^{-3} K^{-1}.

For temperatures approaching the Debye temperature (343 K for Cu), $G(T_e, T_l)$ tends toward a less sharply temperature-dependent reference value, G_{RT}. For copper near 300 K, a value of $G_{\mathrm{RT}} = 9.0 \times 10^{16}$ W m^{-3} K^{-1} is adopted, consistent with pump-probe experimental results [31,32] and the baseline G_0 derived from density functional theory calculations before strong electron temperature effects dominate [33]. While some models predict a decrease in G for electron temperatures far exceeding the Debye temperature [33], treating G_{RT} as a constant saturation value is a valid approximation for the temperature regimes relevant to this work.

To our knowledge, there are no experimental or theoretical predictions of $G(T_e, T_l)$ for Cu continuously from sub-Kelvin to room temperature. To provide a smooth transition across the entire temperature range from the low-temperature power-law behavior to the higher-temperature reference value, two limiting forms are combined using a generalized mean:

$$G(T_e, T_l) = \{[G_{\mathrm{low}}(T_e, T_l)]^{-n_b} + (G_{\mathrm{RT}})^{-n_b}\}^{-1/n_b}, \quad (6)$$

with a bridging exponent $n_b = 4$ chosen to provide a smooth and monotonic transition between the two asymptotic regimes as illustrated in Fig. 2. The formulation dictates that G_{low} dominates at temperatures below the natural crossover point (approximately 54 K for $T_e = T_l$), and G_{RT} primarily governs the coupling at higher temperatures.

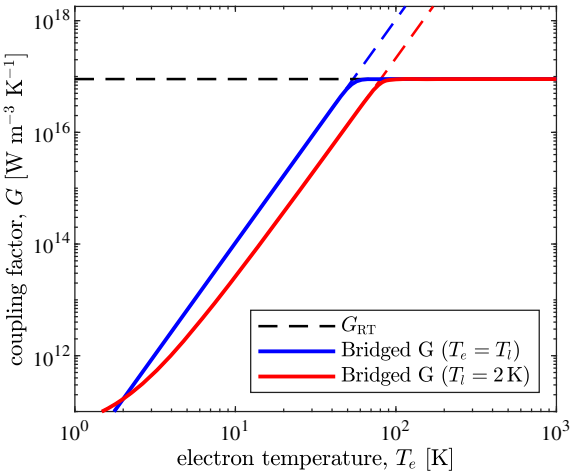

FIG. 2. Electron-phonon coupling factor, G, as a function of electron temperature. It illustrates the behavior of the full bridged model under two limiting conditions: thermal equilibrium ($T_e = T_l$) and strong nonequilibrium ($T_l = 2$ K, varying T_e). The asymptotic low-temperature power-law (G_{low}) and high-temperature saturation (G_{RT}) models are shown for reference.

2. Electron heat capacity C_e

The volumetric heat capacity of the electron gas, $C_e(T_e)$, is commonly approximated at low temperatures by its linear term:

$$C_e(T_e) = \gamma_e T_e, \quad (7)$$

where γ_e is the electronic specific heat coefficient. For copper, $\gamma_e \approx 96.6$ J m^{-3} K^{-2}. The linear approximation provides good accuracy for relatively low electron temperatures, which are relevant to this work. It is worth noting that when electron temperatures T_e become more elevated and approach values in the order of several thousand Kelvin it becomes advisable to introduce higher-order terms from the Sommerfeld expansion to Eq. (7) for improved accuracy [34,35].

3. Lattice heat capacity C_l

The volumetric heat capacity of the lattice is determined using the Debye model [35]:

$$C_l(T_l) = 9 N_a k_B \left(\frac{T_l}{\Theta_D}\right)^3 \times \int_0^{\Theta_D/T_l} \frac{\xi^4 e^\xi}{(e^\xi - 1)^2}\, \mathrm{d}\xi, \quad (8)$$

where $N_a = 8.4912 \times 10^{28}$ m^{-3} is the number density of atoms for copper, k_B is the Boltzmann constant, and $\Theta_D = 343$ K is the Debye temperature for copper.

4. Electrical resistivity ρ_{el}

The total electrical resistivity $\rho_{el}(T_l)$ is determined by the Matthiessen's rule, summing the temperature-independent residual resistivity ρ_0 (due to impurities and defects) and the temperature-dependent phonon contribution $\rho_{ph}(T_l)$ [36]:

$$\rho_{el}(T_l) = \rho_0 + \rho_{ph}(T_l). \quad (9)$$

The residual resistivity $\rho_0 = 5.667 \times 10^{-11}$ Ωm is set corresponding to a residual-resistivity ratio (RRR) of 300, using the reference resistivity of copper at room temperature $\rho_{el}(300\ \mathrm{K}) = 1.7 \times 10^{-8}$ Ωm.

The phonon contribution is described by the Bloch-Grüneisen formula:

$$\rho_{ph}(T_l) = A_{\mathrm{BG}} \left(\frac{T_l}{\Theta_D}\right)^5 \times \int_0^{\Theta_D/T_l} \frac{\xi^5 e^\xi}{(e^\xi - 1)^2}\, \mathrm{d}\xi. \quad (10)$$

Prefactor A_{BG} is determined to ensure that $\rho_0 + \rho_{ph}(300\,\mathrm{K})$ yields the room-temperature value.

5. Electron thermal conductivity K_e

The electron thermal conductivity $K_e(T_e, T_l)$ is derived from the Wiedemann-Franz law [34], relating it to the electrical resistivity:

$$K_e(T_e, T_l) = \frac{L_0 T_e}{\rho_{el}(T_l)}, \tag{11}$$

where $L_0 = 2.44 \times 10^{-8}\ \mathrm{W\,\Omega\,K^{-2}}$ is the Lorenz number. The lattice temperature dependence enters through the electrical resistivity $\rho_{el}(T_l)$.

B. Laser source term

The volumetric power density $S_{\mathrm{laser}}(x,t)$ deposited by the laser into the electron system is described by a Gaussian temporal profile with an exponential decay in depth according to the Beer-Lambert law:

$$S_{\mathrm{laser}}(x,t) = \frac{F_{\mathrm{abs}}}{d_p} \frac{1}{\sigma_t \sqrt{2\pi}} \exp\left[-\frac{(t-t_c)^2}{2\sigma_t^2}\right] \exp\left(-\frac{x}{d_p}\right), \tag{12}$$

where F_{abs} is the absorbed laser fluence, d_p is the effective penetration depth, σ_t is the rms pulse duration, and t_c is the time corresponding to the pulse peak. The variables x and t represent the depth into the material and the time, respectively.

In Eq. (12), we assume a Gaussian temporal pulse shape. While actual photoinjector laser pulses can also exhibit other forms (such as flattop), this choice provides a simple analytical description and is sufficient for the present thermal analysis, which primarily targets time-averaged stability of the macroscopic model. For pulses with the same FWHM duration and total energy, the peak surface temperature and the time-averaged heat flux are only weakly sensitive to the detailed temporal shape. However, the pulse shape will affect near-surface temperature distribution.

C. Numerical solution of 1D-TTM

The simulation models the interaction of a single laser pulse with a copper surface in 1D. Equations (2) and (3) were defined as custom partial differential equations and solved in COMSOL Multiphysics® v6.3 using the adaptive backward differentiation formula solver. A nonuniform mesh resolves the optical penetration depth near $x = 0$ and coarsens toward $x = L_x = 50$ μm.

First, let us consider the laser source term [Eq. (12)] with parameters providing a physically representative laser fluence for the 1D-TTM model. We define it based on the operational use case at the future cw European XFEL [5]. For a design specification QE of 2.5×10^{-4}, generating 100 pC electron bunches at a 1 MHz repetition rate corresponds to an average laser power of 2 W (see the right plot in Fig. 1). This implies an incident laser pulse energy of $E_{\mathrm{pulse}} = 2$ μJ (since $P_{\mathrm{avg}} = E_{\mathrm{pulse}} \times f_{\mathrm{rep}}$). The laser spot is treated as having a top-hat intensity profile with a radius of $r_{\mathrm{spot}} = 430$ μm, which corresponds to a spot area $A_{\mathrm{spot}} = \pi r_{\mathrm{spot}}^2$. With a material reflectivity of $R = 0.36$ for copper at an excitation wavelength of 257 nm [37], the absorbed fluence is $F_{\mathrm{abs}} = (1-R)E_{\mathrm{pulse}}/A_{\mathrm{spot}}$. The pulse has an rms duration of $\sigma_t = 8$ ps and its peak is centered at $t_c = 4\sigma_t = 32$ ps. The effective penetration depth d_p, which accounts for both optical absorption and nonthermal electron transport, is taken to be 83 nm. This value is calculated as the sum of the optical penetration depth (≈13 nm) and the ballistic transport range (≈70 nm), an approach proposed for UV excitation of copper in [24]. The left plot in Fig. 3 shows time dependent temperatures of electrons and lattice at $x = 0$. For the relatively long 8 ps rms laser pulse, combined with a low absorbed fluence of 2.2 $\mathrm{J/m^2}$, the 1D-TTM model predicts a modest 6 K difference between the peak electron temperature ($T_e \approx 36.5$ K) and lattice temperature ($T_l \approx 30.5$ K).

For the considered design parameter set of the cw photoinjector for the European XFEL, the 1D-TTM does not predict a significant temperature growth and the observed thermal nonequilibrium is modest. It should be noted that the assumed QE is optimistic. Factors such as a larger pulse energy, a smaller laser spot size, and a shorter pulse duration can have a significant impact on the electron lattice thermal behavior. For example, the right plot in Fig. 3 shows the time-dependent electron and lattice temperatures at $x = 0$ for a laser spot radius of $r_{\mathrm{spot}} = 215$ μm, which is half of the nominal value.

D. Discussion of the results obtained using the 1D-TTM

The TTM is predicated on the assumption that following photon absorption, the electron subsystem thermalizes internally via electron-electron scattering on a timescale τ_{e-e}, that is much shorter than the timescale for electron-phonon energy transfer τ_{e-ph}. This condition ($\tau_{e-e} \ll \tau_{e-ph}$) ensures the existence of a well-defined, quasiequilibrium electron temperature T_e. This assumption is known to be challenged under conditions of very low excitation intensity or with ultrashort (femtosecond) laser pulses. In such cases, the electron distribution may remain nonthermal (i.e., non-Fermi-Dirac) for a period comparable to τ_{e-ph}, making the concept of an electronic temperature technically ill-defined and requiring more fundamental models, such as the Boltzmann transport, for a rigorous description [38]. Furthermore, at cryogenic range of T_l, the applicability of TTM becomes more fragile: under low fluence and femtosecond excitation, experiments on noble metals showed thermal behavior incompatible with TTM because the electron distribution can remain nonthermal on timescales comparable or longer than excitation source [39]. For such operational conditions, the TTM model can be extended by introducing an additional

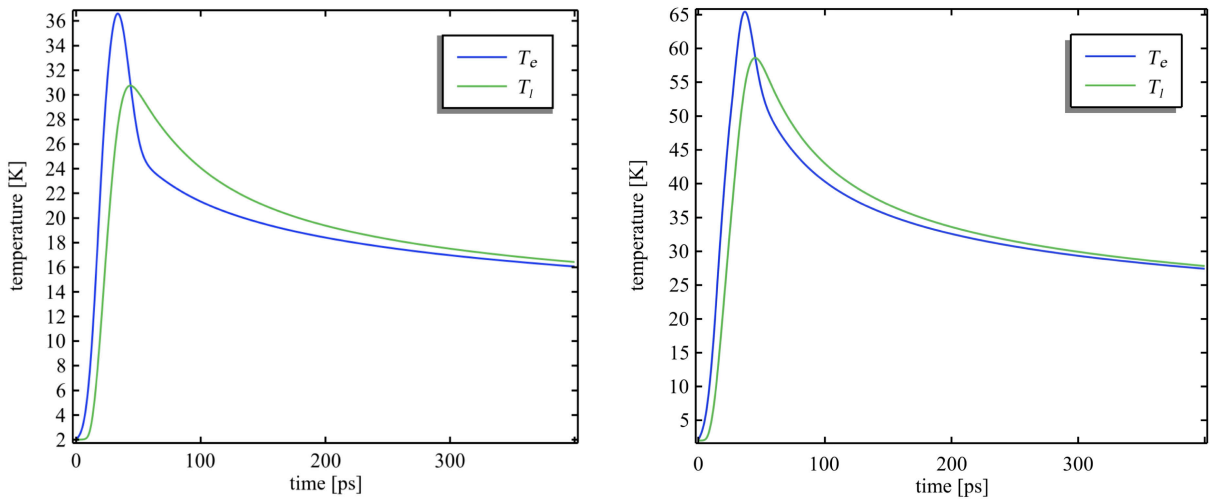

FIG. 3. Temporal evolution of electron (T_e) and lattice (T_l) temperatures at the surface of a copper photocathode, initially at $T_0 = 2$ K. The thermal response is shown for two absorbed laser fluences for the same pulse energy and rms duration $\sigma_t = 8$ ps. Left (nominal parameters): absorbed fluence $F_{\text{abs}} = 2.2$ J/m^2 for a top-hat spot with radius $r_{\text{spot}} = 430$ μm. Right: absorbed fluence $F_{\text{abs}} = 8.8$ J/m^2 obtained by reducing the spot radius by a factor of 2 to $r_{\text{spot}} = 215$ μm.

nonthermal electron reservoir U_{nt} to account for finite thermalization effects [40–42].

However, the laser pulse relevant to this work is on the picosecond scale ($\sigma_t = 8$ ps; FWHM ≈ 19 ps). This pulse duration is significantly longer than the subpicoseconds timescales typically associated with electron thermalization in noble metals. The laser does not act as an instantaneous impulse, but rather as a continuous heating source over a period comparable to, or longer than, the internal relaxation times. This allows a quasiequilibrium state to be established and maintained, where the electron subsystem is simultaneously heated by the laser, thermalized by electron-electron scattering, and cooled by the lattice. In this regime, the TTM serves as a valid and physically appropriate model for describing the average energy balance and the coupled thermal dynamics of the electron and lattice subsystems on the relevant picosecond timescale.

The purpose of 1D-TTM in this work is twofold. First, it demonstrates that for the operational parameters of the cw photoinjector, the peak surface temperatures remain modest in the cryogenic range and the nonequilibrium is minimal at the nominal laser fluence. Second, we define an interface at a depth x_{int} within the 1D TTM domain and calculate the net conductive heat flux crossing the plane. The flux represents the total energy per unit area and time that propagates from the highly nonequilibrium surface layer into the more equilibrated bulk. The resulting time-dependent heat flux serves as a heat source for the macroscopic model. The net flux is the sum of the electronic and lattice contributions:

$$q_{\text{net}}(t) = \left[-K_e(T_e, T_l)\frac{\partial T_e}{\partial x} - K_l(T_l)\frac{\partial T_l}{\partial x}\right]\Bigg|_{x=x_{\text{int}}} \tag{13}$$

Here, $x_{\text{int}} = 2$ μm is chosen as the interface between the highly nonequilibrium surface layer and the diffusive bulk. This depth lies well beyond the effective laser absorption region ($d_p = 83$ μm, which accounts for both optical absorption and ballistic electron range), so that thermal transport at x_{int} is predominantly diffusive. In practice, x_{int} was selected as the smallest depth at which the time-dependent heat-flux profile $q_{\text{net}}(t)$ becomes smooth and the electron and lattice temperatures have essentially converged. Choosing planes closer to the surface yields flux profiles that are dominated by the steep electron-temperature gradient and exhibit pronounced nonequilibrium structure. Increasing x_{int} further (e.g., from 3 to 5 μm) does not change the integral of $q_{\text{net}}(t)$, but only delays its arrival in time. A sufficiently long simulation time was used to verify global energy conservation at the chosen interface depth.

Comparing the temporal distribution of $q_{\text{net}}(t)$ derived from the 1D-TTM to the incident laser's Gaussian profile (Fig. 4) reveals that the TTM-based heat source represents a more physically realistic heat deposition, with a more gradual temporal distribution that accounts for the intrinsic energy transfer time within the material.

III. TWO-DIMENSIONAL TRANSIENT AND STATIONARY THERMAL ANALYSIS OF A BULK COPPER PHOTOCATHODE

We characterize the temperature of the bulk cathode with the aim to validate a steady-state approach for subsequent 3D analysis. For timescales significantly longer than the electron-phonon relaxation time, the thermal behavior

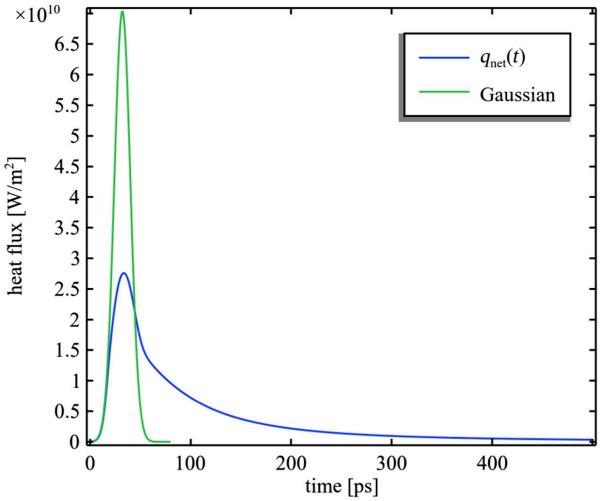

FIG. 4. Qualitative comparison of temporal distribution of the heat flux derived from the TTM and a standard 8 ps rms Gaussian laser pulse. Both correspond to a total absorbed pulse energy 2 μJ × $(1 - R) = 1.28$ μJ, where $R = 0.36$ is the copper reflectivity.

within the bulk copper is described by the classical heat conduction equation:

$$\rho(T)C_p(T)\frac{\partial T}{\partial t} = \nabla \cdot (k(T)\nabla T) + Q_{\mathrm{vol}}(r, z, t), \qquad (14)$$

where $T(r, z, t)$ is the temperature field as a function of the radial coordinate r, the axial coordinate z, and the time t; ρ is the material density; $C_p(T)$ is the temperature-dependent specific heat capacity; $k(T)$ is the temperature-dependent thermal conductivity; and Q_{vol} is the volumetric heat source. For the bulk model, the temperature-dependent thermal conductivity $k(T)$ and specific heat capacity $C_p(T)$ are implemented using polynomial fits to cryogenic reference data for copper (RRR = 300) from [43]. The left plot in Fig. 5 shows the corresponding thermal conductivity of Cu for various RRR values, with the solid line representing the data used for the bulk cathode modeling. For comparison, we show K_e obtained in Sec. II A assuming $T_e = T_l$. The discrepancy arises because our theoretical model calculates the conductivity from idealized physical laws, while the NIST data are based on a polynomial fit that relies on experimental measurements. The right plot in Fig. 5 illustrates the specific heat capacity as a function of temperature for Cu. While the density ρ also exhibits a temperature dependence, its variation for solid-state copper is minimal, and a constant room-temperature value of $\rho = 8960\ \mathrm{kg\,m^{-3}}$ is assumed.

Solving the time-domain heat transfer model for a 1 MHz repetition rate with picosecond laser pulse duration is computationally expensive. In such cases, a stationary model offers a significantly simplified analysis. The steady-state solution assumes neglect of the time derivative in Eq. (14) and replacement the pulsed heat source with its time-averaged equivalent boundary condition. The primary goal of the subsequent analysis is to validate the steady-state simulation approach by directly comparing its results to those from a full transient simulation.

A. Validation of the steady-state approach

We validate the steady-state approach by using a simplified two-dimensional, axially symmetric model with the boundary conditions as shown in Fig. 6.

We begin by solving the transient heat conduction problem described by Eq. (14). The heat source from the laser is modeled as a periodic boundary heat flux

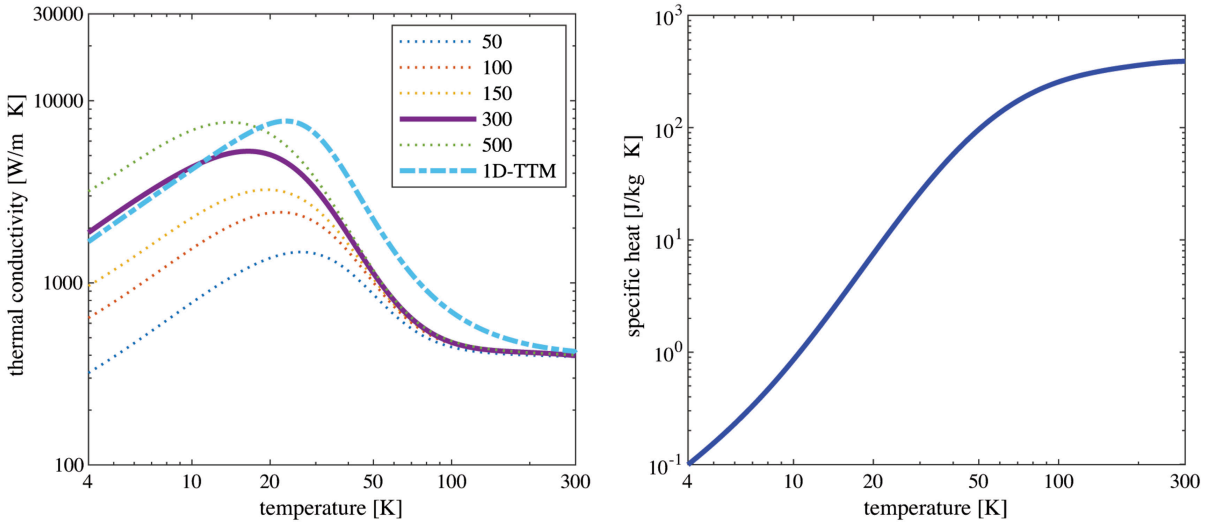

FIG. 5. Left plot shows the thermal conductivity of copper as a function of temperature for various values of RRR. The solid line (RRR = 300) represents the NIST fit used in the bulk model. The dashed line shows the conductivity derived from the TTM components for comparison. The right plot presents the specific heat capacity of copper as a function of temperature.

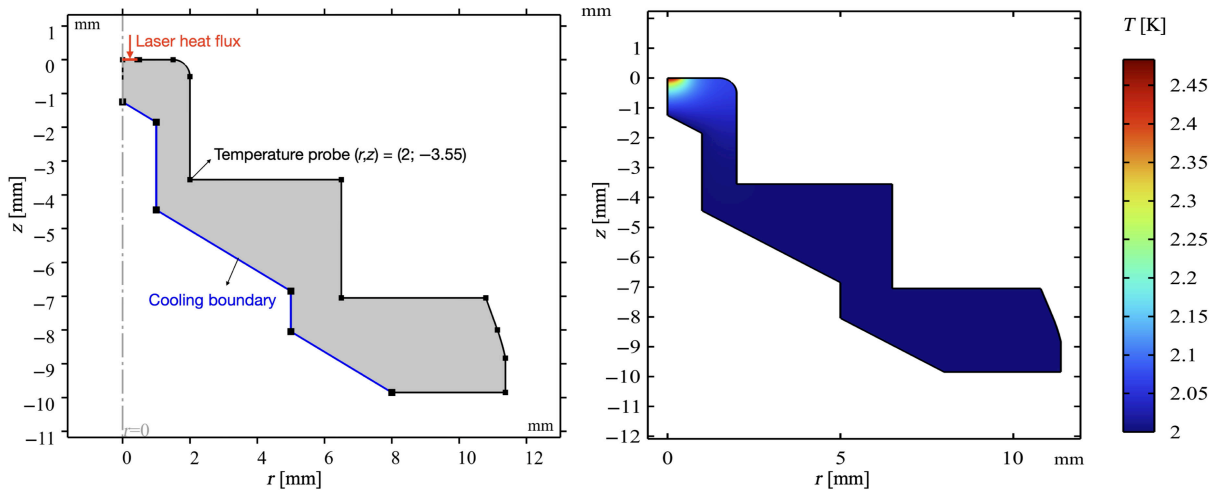

FIG. 6. Left image shows the simplified axially symmetric representation of the Cu cathode plug with partially indicated boundary conditions: blue cooling boundary, red laser heat flux, and remaining boundaries set to Neumann boundary condition. The right image presents the steady-state temperature distribution in the model with ideal cooling, for an average incident laser power of 2 W.

applied at the cathode emission surface ($z = 0$, $r \leq r_{\text{spot}} = 430$ μm)

$$-\mathbf{n} \cdot (k\nabla T) = q_{\text{net}}(t), \tag{15}$$

where $q_{\text{net}}(t)$ is the time-dependent heat-flux profile obtained from the 1D-TTM analysis, as defined in Eq. (13), and $\mathbf{n}$ is the normal vector to the surface. A primary challenge in achieving a numerical convergence of the solution in the time domain is resolving steep thermal gradients near the boundary where the heat flux is applied. To address this, a locally refined mesh is used within the boundary layer region, where the solution varies significantly, as illustrated in Fig. 7.

Next, we solve the corresponding steady-state problem using a time-averaged inward heat flux boundary condition:

$$-\mathbf{n} \cdot (k\nabla T) = q_{\text{avg}}, \qquad q_{\text{avg}} = P_{\text{avg}}(1 - R)/A_{\text{spot}}, \tag{16}$$

where P_{avg} denotes the incident laser power, and $R = 0.36$ is the copper reflectivity.

Figure 8 shows the transient solution, where the temperature evolution is evaluated at the point of interest $(r, z) = (2\text{ mm}, -3.55\text{ mm})$ (see Fig. 6). This location is the closest point between the heat source and the copper domain adjacent to the indium-sealed Cu-In-Nb interface, where heat is transferred from the cathode into the niobium cavity. It is therefore used as a representative point to compare the time-dependent and stationary solutions. After a ramp-up period of approximately 6 μs, the temperature stabilizes into an oscillation with a mean value of 2.0014 K.

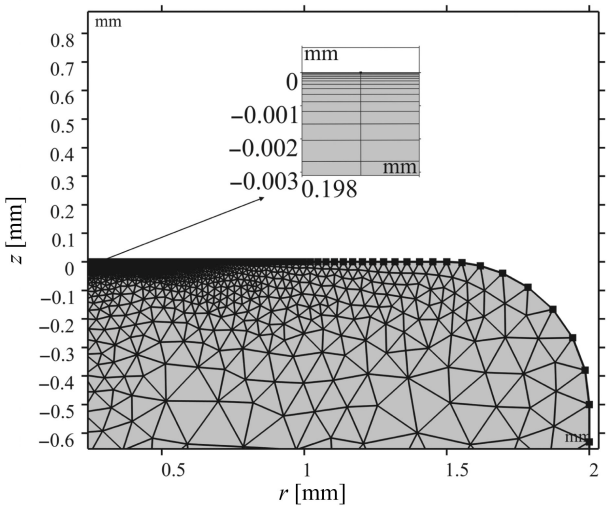

FIG. 7. Mesh refinement at the boundary layer near the laser heat flux boundary condition.

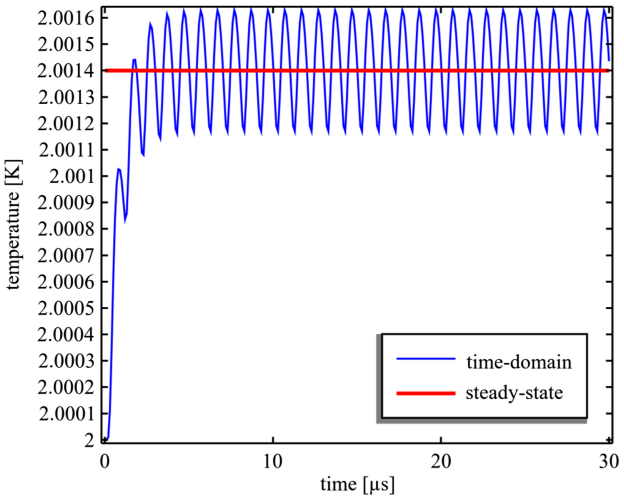

FIG. 8. Temperature versus time from the transient model, probed at the foreseen initial Cu-In-Nb contact point ($r = 2$, $z = -3.55$) under ideal cooling ($T_0 = 2$ K) and periodic 1 MHz laser heating with 2 μJ incident energy per pulse.

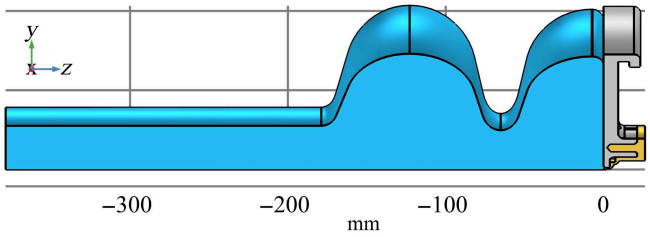

FIG. 9. 1.6-cell SRF injector's 3D model for coupled rf-thermal analysis. The axially symmetric section (1/8) shows the Cu plug (yellow), the Nb back wall (gray), and the rf vacuum volume (blue).

The steady-state solution at the same point is 2.0014 K, thus matching precisely the transient result. This comparison indicates that the thermal time constant of the bulk cathode is significantly longer than the pulse period, causing the material to respond primarily to the average power input.

This validation confirms that the computationally efficient steady-state model is sufficient for determining the mean operational temperatures of the bulk cathode. For the initial comparative study, an ideal cooling condition ($T = 2$ K) was imposed to ensure numerically fast thermal equilibration in the transient solution. In the subsequent analysis, we use the steady-state approach to study a physically realistic thermal model that incorporates the dominant thermal impedance of the Kapitza boundary resistance at the helium-cooled surfaces [44].

IV. THREE-DIMENSIONAL COUPLED THERMAL-ELECTROMAGNETIC ANALYSIS

A central concern for the integrated cathode design is whether the laser-induced heat load negatively affects the injector cavity's thermal and electromagnetic stability. A three-dimensional (3D) steady-state model is developed to evaluate two primary operational limits of the integrated cathode design under laser heat load. The first is a cryogenic stability at Cu-He interface. The second risk factor arises from a positive thermal feedback loop, where heat conducted from the cathode increases the niobium's temperature-dependent surface resistance $R_s(T)$, thus amplifying the local rf power dissipation, which directly impacts the cavity's quality factor. On the other hand, the structure of the TM_{010} accelerating electromagnetic mode features a minimal magnetic field responsible for rf losses in the region of niobium, which is affected by laser heat deposited from the cathode. To determine which effect dominates, we developed and solved a 3D steady-state coupled thermal-electromagnetic model.

A. Thermal-electromagnetic model definition

The computational model, shown in Fig. 9, consists of the copper photocathode plug, the niobium cavity back wall, and the rf vacuum volume. A 1/8th section of the geometry is simulated due to the partial axial symmetry of the back wall's mechanical design. A schematic illustrating computational domains and boundary conditions is shown in the left image of Fig. 10.

The thermal analysis is governed by the steady-state heat version of equation Eq. (14). The laser heat is introduced as an inward heat flux boundary condition as defined in Eq. (16), evaluated for an average incident laser power P_{avg}. The temperature-dependent thermal conductivities for copper (RRR = 300, Sec. III) and niobium (RRR = 300, shown in the left plot of Fig. 11) are used. A primary heat transfer path from the cathode to the niobium is the Cu-In-Nb contact, which is characterized by a thermal contact resistance R_{tc}. Specific experimental data for the thermal contact resistance of a Cu-In-Nb connection are not readily available. We therefore describe this interface using a value derived from experimental measurements of a similar pressed Nb-In-Al joint, for which Dhuley *et al.* report a contact resistance of $R_{tc} \approx 1.0 \times 10^{-4}$ K m^2 W^{-1} at a

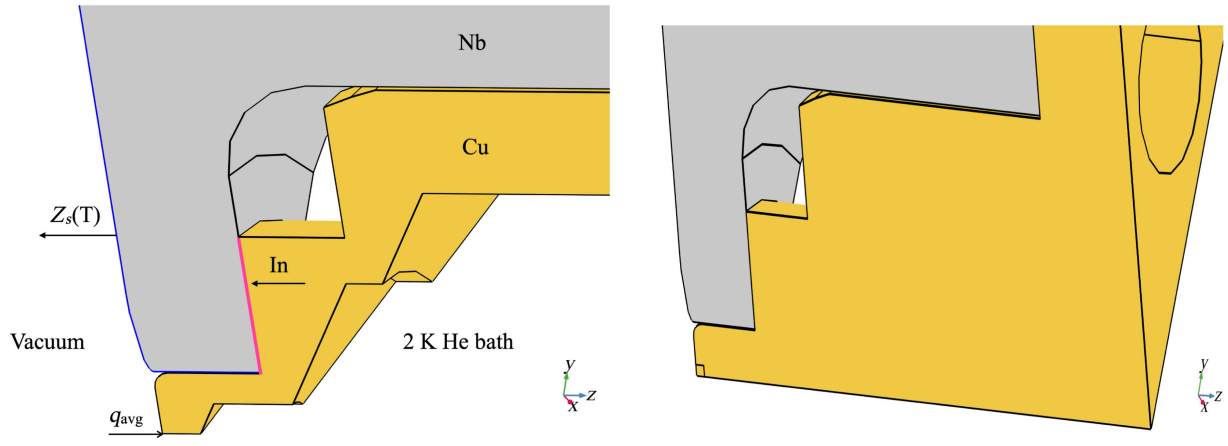

FIG. 10. Image on the left shows the schematic of the domains and principal boundary conditions in the 3D model at the Cu-Nb interface. The image on the right presents the improved copper cathode plug geometry (yellow).

temperature of 4.2 K [45]. The validity of extrapolating from Nb-In-Al to Cu-In-Nb is based on the physics of thermal transport in such assemblies at liquid helium temperatures. In this regime, heat transfer across metal-metal joints with an indium interlayer is dominated by phonons: the main thermal resistance arises in the indium layer and at the two metal-indium interfaces, while the bulk resistance of the outer metals (Cu, Al, Nb) is small due to their higher thermal conductivities. For comparable joint geometry, indium thickness and contact pressure, Nb-In-Al and Cu-In-Nb contacts are therefore expected to exhibit similar area-specific thermal contact resistances. Moreover, since high-purity copper has a higher thermal conductivity than aluminum in the 2–4 K range, the constriction resistance on the aluminum side is larger, so using the Nb-In-Al value for Cu-In-Nb is conservative. Dhuley *et al.* experimentally demonstrate that the thermal resistance of these pressed joints follows a near cubic dependence on temperature, $R_{tc} \propto T^{-3}$, consistent with phonon-dominated interfacial transport at cryogenic temperatures and with diffuse mismatch model predictions. For the present analysis, we therefore adopt an extrapolated conservative estimate for the area-specific contact resistance of the Cu-In-Nb joint, $R_{tc,\text{Cu-In-Nb}}(2\,\text{K}) \approx 1.0 \times 10 - 3\,\text{K}\,\text{m}^2\,\text{W}^{-1}$. Since this value is not directly measured for our specific joint configuration, we have performed a sensitivity analysis of the model with respect to variations of R_{tc} (Sec. IV D), which shows only a weak influence on the thermal figures of merit considered in this work. This thermal resistance is applied at the indium-sealed interfaces as a thermal contact resistance boundary condition without directly introducing indium into the computational domain. This imposes a temperature discontinuity $\Delta T = T_u - T_d$ that is proportional to the normal heat flux q_n flowing across the interface:

$$q_n = \mathbf{n} \cdot (-k\nabla T), \qquad T_u - T_d = q_n R_{tc}, \tag{17}$$

where T_u and T_d are the temperatures on the upstream and downstream sides of the boundary, respectively. R_{tc} is the area-specific thermal contact resistance and the heat flux q_n is continuous across the boundary.

The cooling regime at the Cu-He II and the Nb-He II is governed by the Kapitza conductance $h_K = aT^3$, a phenomenon of phonon transport across a boundary. The standard physical model for this process across a temperature difference is provided by the modified acoustic mismatch theory [44]. Table I summarizes typical experimental values for the prefactor a [$\text{W}\,\text{m}^{-2}\,\text{K}^{-4}$]. For the copper photocathode in our model, we assume a clean surface while for the niobium cavity, we use a value representative of a standard buffered chemical polish (BCP) finish. It is often convenient to describe this boundary impedance in terms of the Kapitza thermal resistance $R_K(T) = [h_K(T)]^{-1}$. The temperature-dependent

TABLE I. Kapitza conductance coefficient, a, for Cu-He IInd Nb-He II, where the heat conductance is $h_K = aT^3$ at $T \approx 2$ K. Values are representative midpoints compiled from the literature.

Material	Surface condition	a ($\text{W}\,\text{m}^{-2}\,\text{K}^{-4}$)
Copper	Clean	1.0×10^{3}[a]
	Technical	5.0×10^{2}[b]
	Rough	2.0×10^{2}[a]
Niobium	Electropolished	1.0×10^{3}[c]
	BCP cavity-grade	4.0×10^{2}[d]
	Rough	2.0×10^{2}[d]

[a]Lebrun and Tavian [47].
[b]Swartz and Pohl [44].
[c]Amrit *et al.* [48].
[d]Aizaz *et al.* [49] and Dhakal *et al.* [50].

Kapitza resistance is implemented as the cooling boundary condition for the steady-state thermal analysis:

$$q = -\mathbf{n} \cdot (k\nabla T) = \frac{T - T_{\text{bath}}}{R_K}, \tag{18}$$

where $\mathbf{n}$ is the normal vector, T is the local surface temperature, and $T_{\text{bath}} = 2$ K is the helium bath temperature.

The computed steady-state temperature distribution provides the input for the electromagnetic eigenmode analysis. The coupling to the electromagnetic computation domain is implemented through a surface impedance boundary condition with impedance $Z_s(T) = R_s(T) + iX_s(T)$ applied at the backwall of the cavity. The remaining boundaries for the EM problem are treated as perfect electric conductors. The surface reactance X_s is calculated for niobium at a frequency $f = 1.3$ GHz using the London penetration depth approximation $X_s \approx \omega\mu_0\lambda_L \approx 0.40$ mΩ, where the angular frequency is $\omega = 2\pi f$, μ_0 is the permeability of free space, and the London penetration depth is taken as $\lambda_L \approx 39$ nm. While temperature dependent, X_s is approximated as a constant value due to the localized domain affected by cathode laser heating. The resistive component $R_s(T)$ is the sum of a residual component R_{res} and the BCS resistance, given by

$$R_{\text{BCS}}(T) = \frac{C}{T} f^2 \exp\left(-\frac{\Delta(T)}{k_B T}\right). \tag{19}$$

The superconducting energy gap, $\Delta(T)$, is computed using the Muhlschlegel approximation with $T_c = 9.25$ K and $\Delta(0)/k_B T_c = 1.9$. The free parameters, C and R_{res}, were determined via a direct fit to measurements of the cw SRF injector cavity at DESY (16G09) (the right plot of Fig. 11), yielding $R_{\text{res}} = 8.3$ nΩ and $C = 31182$ nΩ K/GHz^2.

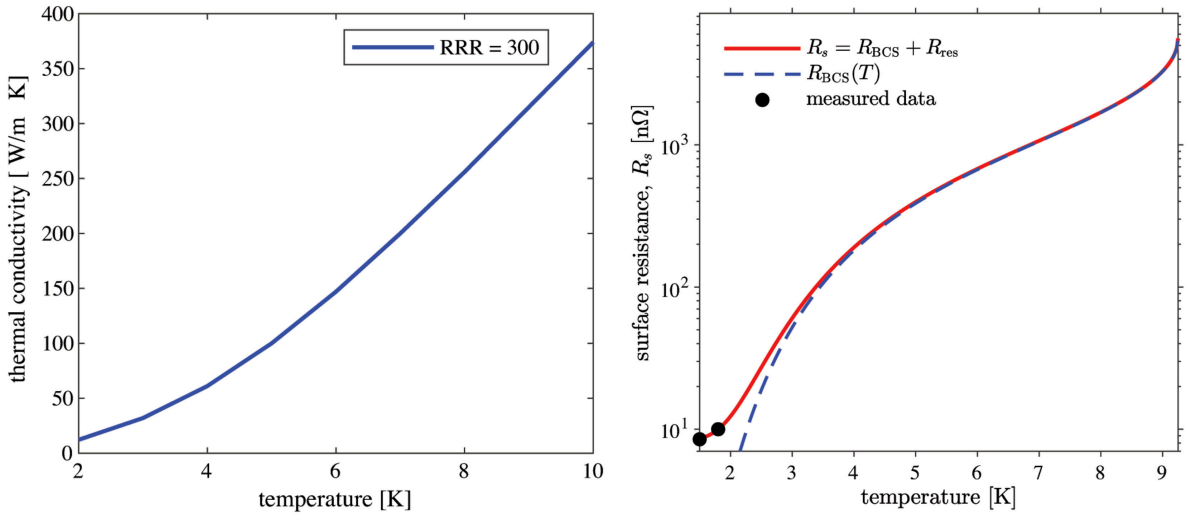

FIG. 11. Left plot shows the thermal conductivity of niobium (RRR = 300) versus temperature [46]. The right plot presents the surface resistance of niobium at 1.3 GHz. Points are experimental data for the DESY 16G09 cavity; the red line is the model fit from Eq. (19).

B. Thermal stability at the copper-helium interface

The analysis of the 3D model with the baseline cathode geometry shown in the left image of Fig. 10 reveals a potential cooling issue. For a nominal incident laser power of 2 W, the steady-state solution predicts that the temperature on the helium-wetted-copper surface exceeds the helium saturation temperature ($T_{sat} \approx 2.0$ K at ∼31 mbar) by $\Delta T = T_{peak} - T_{sat} \approx 0.4$ K. The left image in Fig. 12 illustrates this for an incident laser power of 2 W, indicating a localized hot spot on a conical protrusion reaching approximately 2.4 K. Here $T_{peak} \approx 2.4$ K denotes the copper temperature, while the helium side is numerically fixed at $T_{bath} = T_{sat} = 2$ K by the Kapitza-to-bath boundary in Eq. (18). This boundary condition is only valid for single-phase He-II. However, helium boiling can arise when the helium-side peak heat flux limit is approached or exceeded, with the threshold depending on geometry and immersion depth [51,52]. Within this modeling framework, the magnitude of ΔT is used as a conservative indicator of a thermally loaded interface where two-phase effects could potentially develop at the indicated hot spot. The present model indicates risk but does not predict onset or the critical heat flux.

The potential onset of two-phase effects fundamentally alters the heat transfer mechanism from efficient solid-to-superfluid conduction to less predictable two-phase regime. The primary concern in this regime is the onset of film boiling, which insulates the hot spot with a layer of helium vapor. If the insulating vapor film propagates, heat transport into the helium bath can be strongly reduced and a larger fraction of the load conducts into the SRF injector's niobium structure. Furthermore, sustained boiling dynamics near a high-Q SRF cavity

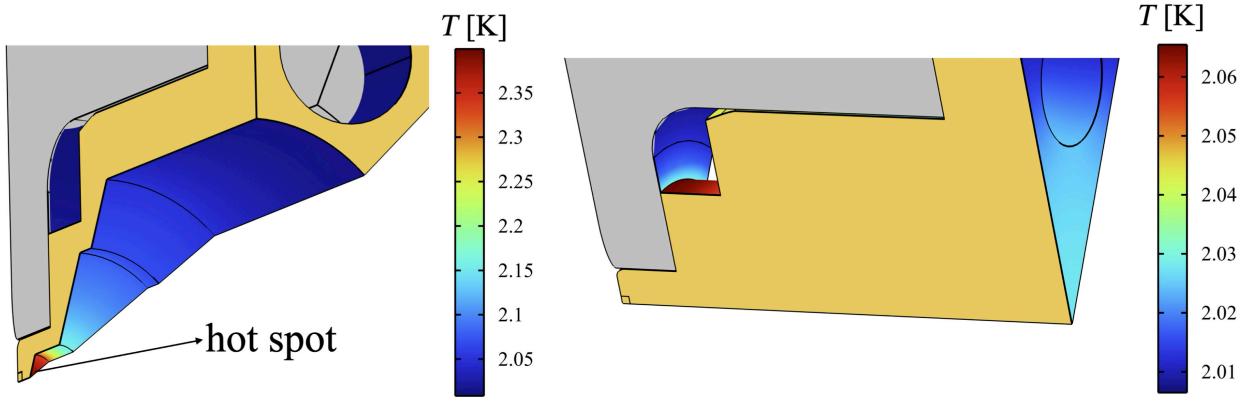

FIG. 12. Image on the left shows the steady-state temperature distribution on the helium-wetted surfaces of the copper plug and adjacent niobium back wall, for an incident laser power of 2 W. The image on the right presents the steady-state temperature distribution on the helium-wetted surfaces of the improved version of the copper plug and adjacent niobium back wall, for an incident laser power of 2 W.

introduces a secondary parasitic effect, i.e., it leads to thermomechanical vibrations [53].

The thermal performance of the baseline plug geometry is constrained by a conductive bottleneck within the plug geometry. While cooling at the boundary is initially governed by Kapitza resistance, the narrow cross section of the protrusion creates a significant internal thermal impedance. This impedance concentrates the heat flux, leading to the localized temperature rise before heat can be effectively distributed across the wetted interface. An alternative cathode plug geometry, shown conceptually in the right image of Fig. 10, was evaluated to address this conductive limitation. The modification increases the local cross section in the vicinity of the hot spot, providing a lower impedance path for lateral heat conduction that more effectively distributes the thermal load.

The 3D steady-state model was solved for the improved geometry. The right image in Fig. 12 shows the resulting temperature distribution at the cooling surfaces for a nominal incident laser power of $P_{\mathrm{avg}} = 2$ W. For this case, the peak temperature of the copper cathode at the helium interface is $T_{\mathrm{peak}} \approx 2.07$ K, and the corresponding heat flux is approximately 550 W/m^2 (single-phase Kapitza boundary flux). The 70 mK temperature rise is modest and the wetted-copper surface temperature remains near saturation temperature. We then evaluated a higher heat-load case with an average incident laser power of $P_{\mathrm{avg}} = 5$ W. The simulation predicts a peak helium-wetted surface temperature of $T_{\mathrm{peak}} \approx 2.14$ K. For the subsequent rf analysis, we treat the 5 W temperature field as single-phase cooling and assume that the Kapitza boundary condition remains valid.

C. Laser heating and rf performance

We now evaluate the impact of the laser induced temperature gradients on the rf performance of the injector cavity with improved geometry of the Cu cathode plug (see Fig. 10, right). The analysis solves the stationary, coupled thermal-electromagnetic model to determine, if the localized heating of the niobium back wall leads to an increase in dissipated rf power.

First, the thermal model is solved for incident laser powers of 2 and 5 W. The temperature field is then used to compute the local surface resistance, shown on the left in Fig. 13, where a modest increase is observed near the central axis. Despite the moderate laser induced thermal load of the injector cavity, given the exponential dependence of the BCS resistance on temperature, a multistep iterative analysis was performed to ensure that the initial temperature rise does not trigger a thermal feedback runaway. The calculated rf losses were added back into the thermal model as a heat source, and the loop was repeated 4 times. The results, shown in Fig. 14, demonstrate immediate convergence after the second iteration, confirming the thermal feedback is negligible and the system is electromagnetically stable. The image on the right in Fig. 14 presents the steady-state temperature distribution in the copper photocathode plug, based on the solution of the fourth iteration of the coupled rf-thermal model for an incident laser power of $P_{\mathrm{avg}} = 5$ W.

The temperature distribution in the system is dictated by the copper cathode plug, resulting in a modest temperature rise in the vicinity of the cathode opening of the injector cavity. Moreover, the magnetic field of the TM$_{010}$ π mode on the interior of the injector's backwall field is zero on the central axis ($r = 0$) and increases with radius.

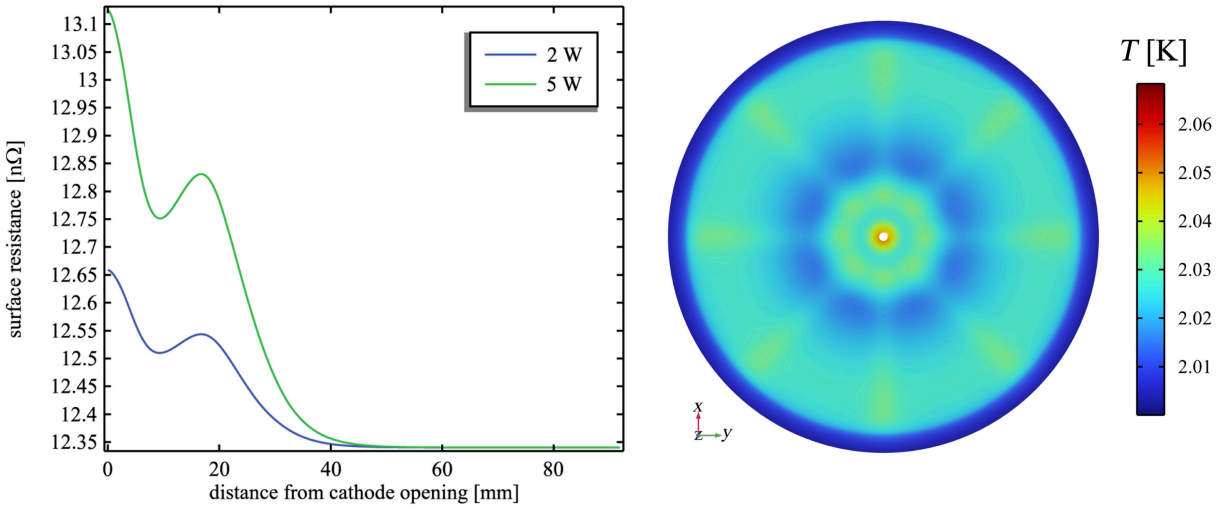

FIG. 13. Left plot shows the local surface resistance along the radius of the niobium back wall, based on the temperature profiles from the thermal model. The image on the right presents the steady-state temperature distribution on the interior surface of the niobium back wall of the injector cavity, based on the solution of the fourth iteration of the coupled rf-thermal model for an incident laser power of $P_{\mathrm{avg}} = 5$ W.

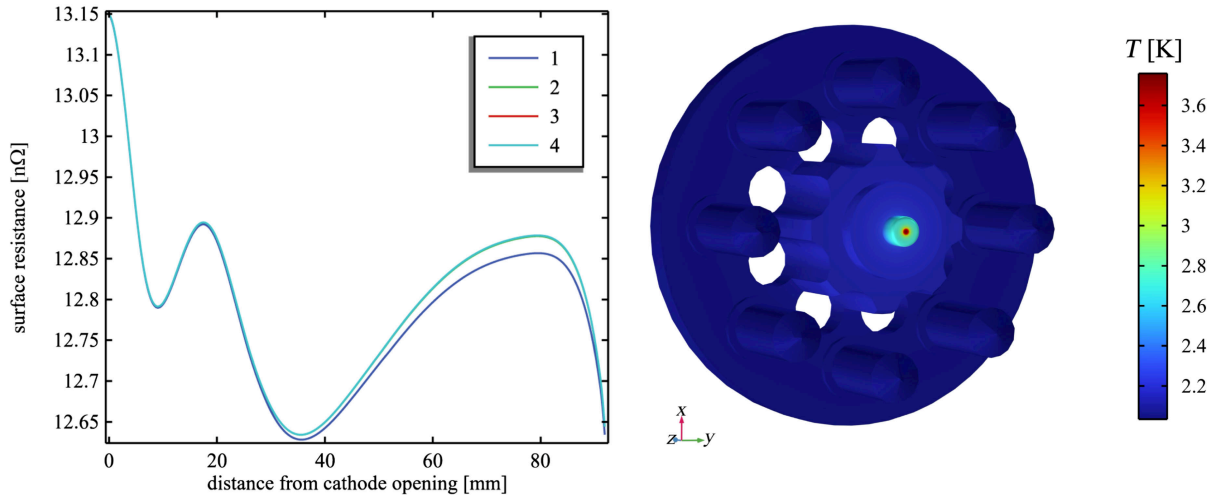

FIG. 14. Left plot shows the surface resistance profiles along the niobium back wall for four consecutive iterations of the coupled thermal-electromagnetic model, calculated for an incident laser power of 5 W. The image on the right presents the steady-state temperature distribution in the copper photocathode plug, based on the solution of the fourth iteration of the coupled rf-thermal model for an incident laser power of $P_{\mathrm{avg}} = 5$ W.

A comparison with the temperature map (the image on the right in Fig. 13) indicates that the area of the maximum temperature increase coincides with the region of low magnetic field. As a result, the integral for total dissipated rf power [Eq. (1)] is dominated by the vast surface areas operating at nominal resistance, rendering the effect of localized heating negligible. Calculating the dissipated power assuming first $T = 2\,\mathrm{K} = \mathrm{const.}$ yields 1.109 W at the backwall of the cavity (0th iteration). Following the fourth iteration of thermal-electromagnetic coupled simulation yields a 2.8% higher dissipated power of 1.14 W, which is mainly driven by the rf load (50 MV/m axial peak electric field) following the temperature rise after the first iteration. Therefore, we conclude that the primary thermal consideration for the injector cavity design is the management of the cryogenic cooling at the Cu-He interface, rather than the rf-thermal feedback.

D. Sensitivity analysis of the Cu-In-Nb joint thermal contact resistance

To quantify the influence of the uncertain Cu-In-Nb contact resistance on the thermal and rf behavior of the gun cavity, we performed a sensitivity study in which R_{tc} was varied over three values: $R_{tc} = 0$, 0.001, and 0.002 K m^2 W^{-1}. These values span from the ideal resistance-free limit ($R_{tc} = 0$) through the nominal conservative

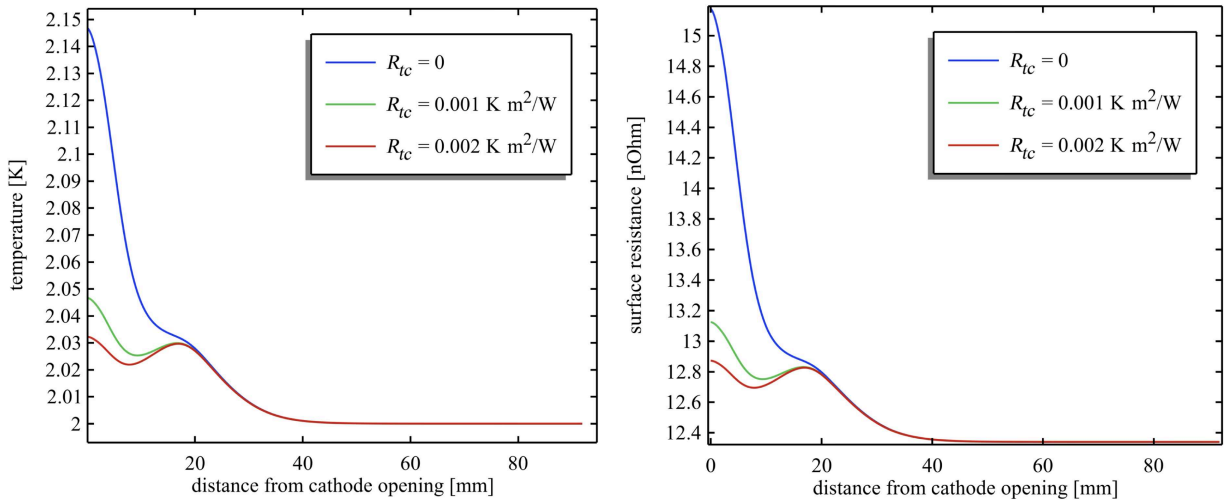

FIG. 15. Sensitivity of the thermal and rf response to the Cu-In-Nb contact resistance. Left: temperature along the niobium back wall as a function of distance from the cathode opening for three values of the contact resistance R_{tc}. Right: corresponding local rf surface resistance obtained from the temperature profiles. In all cases, the effect of R_{tc} is confined to a narrow region around the cathode opening, and the integrated rf power dissipation changes by well below 1%.

estimate $R_{tc,0} = 0.001\ \mathrm{K\,m^2\,W^{-1}}$ to a twofold increase. We consider sensitivity analysis for an incident laser power of 5 W.

Figure 15 shows the resulting temperature and rf surface resistance distributions along the niobium cavity wall. On the niobium side, reducing the contact resistance to $R_{tc} = 0$ increases the peak temperature at the cathode opening to about 2.15 K, whereas increasing it to $0.002\ \mathrm{K\,m^2\,W^{-1}}$ reduces the peak to approximately 2.03 K. This local temperature variation is reflected in the rf surface resistance: the maximum R_s near the opening varies from approximately 15 nΩ for $R_{tc} = 0$ to approximately 12.8 nΩ for $R_{tc} = 0.002\ \mathrm{K\,m^2\,W^{-1}}$, while all curves converge to the same asymptotic value of ≈12.4 nΩ beyond a distance of ∼20 mm. Because the region affected by the contact resistance is confined to a small area around the cathode opening, the integrated rf losses remain essentially unchanged: the total rf power dissipated in the cavity varies by well below 1% over this entire range of considered R_{tc}.

The copper side is even less sensitive to the assumed contact resistance. For the same three values of R_{tc}, the maximum temperature at the helium-wetted copper interface changes only from 2.1494 to 2.1557 K, with the nominal case at 2.1496 K, i.e., a spread of about 6 mK (less than 0.3%). This confirms that the cryogenic stability of the copper cathode is governed primarily by the applied laser load and the helium-side boundary conditions, whereas uncertainties in the Cu-In-Nb contact resistance have only a minor impact on both copper temperature and rf performance.

V. CONCLUSION

In this work, we developed and applied a comprehensive numerical framework to analyze the thermal characteristics of a cryogenically cooled copper photocathode directly integrated into an SRF injector cavity. The ultrafast surface thermal dynamics were characterized using a one-dimensional two-temperature model developed for the cryogenic regime. For the analysis of bulk heat transfer, a steady-state, time-averaged thermal model was validated against full transient simulations, confirming its computational efficiency. Using this steady-state model, a coupled three-dimensional thermal-electromagnetic analysis was performed, incorporating experimentally fitted data for the niobium surface resistance and literature-based estimates for Kapitza conductance at Nb-He II and Cu-He II interfaces.

The analysis identified a potential cryogenic instability in the baseline cathode geometry, where even at the nominal laser power (2 W) it is predicted to heat the helium-wetted Cu interface above the helium saturation temperature by about 0.4 K at the operating bath pressure (∼31 mbar). The improved design was shown to maintain the interface temperature near saturation ($T_{\mathrm{peak}} \approx 2.07$ K $\Delta T \approx 0.07$ K) for the nominal laser power. Operation beyond the nominal load requires dedicated cryogenic analysis (helium-side peak heat flux) and further optimization of the plug geometry to preserve margin against two-phase effects. The precise onset of boiling in He-II depends on the helium-side peak heat flux, which is not predicted by the present model. We have demonstrated that the present design of the cathode plug can benefit from further systematic cryogenic design optimization in order to mitigate potential instabilities related to localized overheating of the helium-wetted-copper surface.

Assuming the cryogenic stability of the Cu photocathode is established, we confirm that the SRF injector remains electromagnetically stable. A multi-iteration analysis of the thermal-rf feedback loop at 5 W shows rapid convergence. This stability is a direct consequence of the TM_{010} mode's magnetic-field zero on the central axis, which minimizes the impact of localized heating on rf power dissipation in the vicinity of the cathode opening. This finding provides an important design validation and indicates that the primary thermal consideration is the management of the direct cryogenic cooling at the cathode rather than rf-thermal feedback effects. While the modified geometry resolves the cryogenic concern at 2 W, stable operation at 5 W is dependent on single-phase cooling at the Cu-He interface. Any practical implementation targeting more than 2 W should prioritize geometry that reduces spreading resistance and increases the effective wetted perimeter, together with surface conditions that maximize the effective Kapitza conductance, in order to retain an adequate thermal margin.

Finally, we note that the present study should be understood as a design oriented analysis rather than a literal prediction of the built system. The underlying problem combines SRF, cryogenic heat transport, and laser driven surface dynamics, and our models necessarily rely on some simplifying assumptions and parameter choices that are favorable but not guaranteed in practice (e.g., interface conductances, material properties, and idealized boundary conditions). In this sense, the simulations are most appropriately used to identify where thermal or cryogenic margins may become critical and to suggest effective directions for mitigation. The results of this work have been independently reviewed and evaluated by the DESY cryogenics group [54], confirming our findings and motivating the modification of the cathode plug geometry. The quantum efficiency values adopted for copper should likewise be viewed as design targets constrained by realistic UV laser power rather than as established performance in cw operation. Furthermore, the proposed workflow can be applied to future studies of more complex cathode assemblies that incorporate separate emitting areas, for example, a threaded Mg photocathode integrated into a base Cu cathode plug, where higher quantum efficiency may be achieved at the expense of less favorable thermal properties.

ACKNOWLEDGMENTS

We thank D. Reschke for providing experimental data on surface resistance and thermal conductivity for the injector cavity, as well as for reading the manuscript and providing valuable comments. We thank A. K. Dhillon for providing critical comments on the cryogenic operating conditions of the SRF injector and the associated helium-II heat-transfer physics. We thank M. Wenskat for fruitful discussions on questions of the cryogenic stability in SRF environment. Authors thank W. Decking and H. Weise for their interest and support of this work. We thank H. Sinn, M. S. Tavakkoly and F. Yang (European XFEL GmbH) for useful discussion on ultrafast laser heating. We thank support team of Comsol Multiphysics GmbH for assistance on technical questions. Work performed in the framework of R&D for future accelerator operation modes at the European XFEL and financed by the European XFEL GmbH.

DATA AVAILABILITY

The data that support the findings of this article are not publicly available. The data are available from the authors upon reasonable request.

[1] W. Decking *et al.*, A MHz-repetition-rate hard x-ray free-electron laser driven by a superconducting linear accelerator, Nat. Photonics **14**, 391 (2020).

[2] R. Brinkmann, E. Schneidmiller, J. Sekutowicz, and M. Yurkov, Prospects for CW and LP operation of the European XFEL in hard x-ray regime, Nucl. Instrum. Methods Phys. Res., Sect. A **768**, 20 (2014).

[3] E. Vogel *et al.*, SRF gun development at DESY, in *Proceedings of the 29th International Linear Accelerator Conference, Beijing, China* (JACoW, Geneva, Switzerland, 2018), MOPO037, 10.18429/JACoW-LINAC2018-MOPO037.

[4] E. Vogel, J. Sekutowicz, D. Bazyl, T. Büttner, B. van der Horst, J. Iversen, D. Klinke, A. Muhs, D. Reschke, S. Sägebarth, P. Schilling, M. Schmökel, L. Steder, J. H. Thie, H. Weise, and M. Wiencek, High gradients at SRF photoinjector cavities with low RRR copper cathode plug screwed to the cavity back wall, arXiv:2310.02974.

[5] D. Bazyl *et al.*, CW operation of the European XFEL: SC-gun injector optimization, S2E calculations and SASE performance, arXiv:2111.01756.

[6] D. Filippetto, P. Musumeci, R. K. Li, B. J. Siwick, M. R. Otto, M. Centurion, and J. P. F. Nunes, Ultrafast electron diffraction: Visualizing dynamic states of matter, Rev. Mod. Phys. **94**, 045004 (2022).

[7] M. Tonouchi, Cutting-edge terahertz technology, Nat. Photonics **1**, 97 (2007).

[8] J. R. Harris *et al.*, Temperature dependence of photoemission from copper and niobium, in *Proceedings of the PAC2013, Pasadena, CA USA* (JACoW, Geneva, Switzerland, 2013), pp. 1184–1186, https://proceedings.jacow.org/PAC2013/papers/thpac19.pdf?n=PAC2013/papers/THPAC19.pdf.

[9] J. Kühn *et al.*, A Cu photocathode for the superconducting RF photoinjector of BERLinPro, in *Proceedings of the 9th International Particle Accelerator Conference (IPAC'18), Vancouver, BC, Canada* (JACoW, Geneva, Switzerland, 2018), pp. 1247–1250, 10.18429/JACoW-IPAC2018-TUPMF002.

[10] S. Karkare, G. Adhikari, W. A. Schroeder, J. K. Nangoi, T. A. Arias, J. Maxson, and H. Padmore, Ultracold electrons via near-threshold photoemission from single-crystal Cu(100), Phys. Rev. Lett. **125**, 054801 (2020).

[11] J. Kühn, N. Al–Saokal, M. Bürger, M. Dirsat, A. Frahm, A. Jankowiak, T. Kamps, G. Klemz, S. Mistry, A. Neumann, and H. Plötz, Thermal load studies on the photocathode insert with exchangeable plug for the BERLinPro SRF–photoinjector, in *Proceedings of the International Conference on RF Superconductivity, SRF2019, Dresden, Germany* (JACoW, Geneva, Switzerland, 2019), p. 705, 10.18429/JACoW-SRF2019-TUP100.

[12] R. A. Kostin, A. Kanareykin, I. V. Gonin, and E. N. Zaplatin, SRF cavity breakdown calculation procedure using FEA-software, in *Proceedings of the International Conference on RF Superconductivity, SRF2015* (JACoW, Whistler, BC, 2015), p. 140.

[13] T. J. Schultheiss, M. Cole, and J. Rathke, Thermal/structural analysis of a SCRF photocathode electron gun cavity, in *Proceedings of the XX International Linac Conference International Linear Accelerator Conference, Monterey, CA, USA* (JACoW, Geneva, Switzerland, 2000).

[14] S. Barbanotti, P. Pierini, K. Jensch, R. Lange, and W. Maschmann, Thermal and structural modeling of the TTF cryomodule cooldown and comparison with experimental data, in *Proceedings of the European Particle Accelerator Conference, EPAC08, Genoa, Italy* (JACoW, Geneva, Switzerland, 2008), WEPD038.

[15] M. H. Awida, I. Gonin, T. Khabiboulline, and V. P. Yakovlev, Modeling of thermal quench in superconducting RF cavities, IEEE Trans. Appl. Supercond. **30**, 1 (2020).

[16] H. Padamsee, J. Knobloch, and T. Hays, *RF Superconductivity for Accelerators*, 2nd ed. (Wiley-VCH, Berlin, Germany, 2008).

[17] T. P. Wangler, *RF Linear Accelerators*, 2nd ed. (Wiley-VCH, Berlin, Germany, 2008).

[18] Light conversion, PHAROS femtosecond lasers (2025), https://lightcon.com/products/pharos-femtosecond-lasers/.

[19] H. J. Qian, C. Li, Y. C. Du, L. X. Yan, J. F. Hua, W. H. Huang, and C. X. Tang, Experimental investigation of thermal emittance components of copper photocathode, Phys. Rev. ST Accel. Beams **15**, 040102 (2012).

[20] T. Noakes *et al.*, Copper photocathodes for the modified 10 Hz gun on the CLARA accelerator, in *Proceedings of the 14th International Particle Accelerator Conference, IPAC2023, Venice, Italy* (JACoW, Geneva, Switzerland, 2023), TUPA032, 10.18429/JACoW-IPAC2023-TUPA032.

[21] COMSOL AB, COMSOL Multiphysics® simulation software (2025), https://www.comsol.com/ [accessed: 2025-08-01].

[22] J. Sekutowicz *et al.*, Cathodes and shape modification of cavity for DESY superconducting photoinjector, arXiv:2507.01658.

[23] S. I. Anisimov, B. L. Kapeliovich, and T. L. Perel'man, Electron emission from metal surfaces exposed to ultrashort laser pulses, J. Exp. Theor. Phys. **39**, 375 (1974), https://ui.adsabs.harvard.edu/abs/1974JETP...39..375A/abstract.

[24] J. Maxson, P. Musumeci, L. Cultrera, S. Karkare, and H. Padmore, Ultrafast laser pulse heating of metallic photocathodes and its contribution to intrinsic emittance, Nucl. Instrum. Methods Phys. Res., Sect. A **865**, 99 (2017).

[25] Z. Tong, S. Li, X. Ruan, and H. Bao, Comprehensive first-principles analysis of phonon thermal conductivity and electron-phonon coupling in different metals, Phys. Rev. B **100**, 144306 (2019).

[26] M. I. Kaganov, I. M. Lifshitz, and L. V. Tanatarov, Relaxation between electrons and the crystalline lattice, Zh. Eksp. Teor. Fiz. **31**, 232 (1956) [Sov. Phys. JETP **4**, 173 (1957)].

[27] P. B. Allen, Theory of thermal relaxation of electrons in metals, Phys. Rev. Lett. **59**, 1460 (1987).

[28] F. C. Wellstood, C. Urbina, and J. Clarke, Hot-electron effects in metals, Phys. Rev. B **49**, 5942 (1994).

[29] F. Giazotto, T. T. Heikkilä, A. Luukanen, A. M. Savin, and J. P. Pekola, Opportunities for mesoscopics in thermometry and refrigeration: Physics and applications, Rev. Mod. Phys. **78**, 217 (2006).

[30] L. B. Wang, O.-P. Saira, D. S. Golubev, and J. P. Pekola, Crossover between electron-phonon and boundary-resistance limits to thermal relaxation in copper films, Phys. Rev. Appl. **12**, 024051 (2019).

[31] M. Z. Mo, V. Becker, B. K. Ofori-Okai, X. Shen, Z. Chen, B. Witte, R. Redmer, R. K. Li, M. Dunning, S. P. Weathersby, X. J. Wang, and S. H. Glenzer, Determination of the electron-lattice coupling strength of copper with ultrafast MeV electron diffraction, Rev. Sci. Instrum. **89**, 10C108 (2018).

[32] J. Hohlfeld, S.-S. Wellershoff, J. Güdde, U. Conrad, V. Jähnke, and E. Matthias, Electron and lattice dynamics following optical excitation of metals, Chem. Phys. **251**, 237 (2000).

[33] Z. Lin, L. V. Zhigilei, and V. Celli, Electron-phonon coupling and electron heat capacity of metals under conditions of strong electron-phonon nonequilibrium, Phys. Rev. B **77**, 075133 (2008).

[34] N. W. Ashcroft and N. D. Mermin, *Solid State Physics* (Holt, Rinehart and Winston, New York, 1976).

[35] C. Kittel, *Introduction to Solid State Physics*, 8th ed. (John Wiley & Sons, Hoboken, NJ, 2005).

[36] J. M. Ziman, *Electrons and Phonons: The Theory of Transport Phenomena in Solids* (Oxford University Press, Oxford, 1960).

[37] P. B. Johnson and R. W. Christy, Optical constants of the noble metals, Phys. Rev. B **6**, 4370 (1972).

[38] B. Rethfeld, A. Kaiser, M. Vicanek, and G. Simon, Ultrafast dynamics of nonequilibrium electrons in metals under femtosecond laser irradiation, Phys. Rev. B **65**, 214303 (2002).

[39] R. H. M. Groeneveld, R. Sprik, and A. Lagendijk, Femtosecond spectroscopy of electron-electron and electron-phonon energy relaxation in Ag and Au, Phys. Rev. B **51**, 11433 (1995).

[40] E. Carpene, Ultrafast laser irradiation of metals: Beyond the two-temperature model, Phys. Rev. B **74**, 024301 (2006).

[41] G. D. Tsibidis, Ultrafast dynamics of non-equilibrium electrons and strain generation under femtosecond laser irradiation of nickel, Appl. Phys. A **124**, 311 (2018).

[42] M. Uehlein, S. T. Weber, and B. Rethfeld, Influence of electronic non-equilibrium on energy distribution and dissipation in aluminum studied with an extended two-temperature model, Nanomater. Nanotechnol. **12**, 1655 (2022).

[43] N. J. Simon, E. S. Drexler, and R. P. Reed, *Properties of Copper and Copper Alloys at Cryogenic Temperatures*, NIST Monograph Vol. 177 (National Institute of Standards and Technology, Gaithersburg, MD, 1992).

[44] E. T. Swartz and R. O. Pohl, Thermal boundary resistance, Rev. Mod. Phys. **61**, 605 (1989).

[45] R. C. Dhuley, M. I. Geelhoed, and J. C. T. Thangaraj, Thermal resistance of pressed contacts of aluminum and niobium at liquid helium temperatures, Cryogenics **93**, 86 (2018).

[46] T. Schilcher, Wärmeleitvermögen von Niob bei kryogenischen Temperaturen, Diplomarbeit, Universität Regensburg/DESY, 1995; TESLA Report No. 1995-12, in German.

[47] P. Lebrun and L. Tavian, Cooling with superfluid helium, arXiv:1501.07156.

[48] J. Amrit and M. X. François, Heat flow at the niobium-superfluid helium interface: Kapitza resistance and superconducting cavities, J. Low Temp. Phys. **119**, 27 (2000).

[49] A. Aizaz, T. L. Grimm, and N. T. Wright, Thermal design studies in superconducting rf cavities: Phonon peak and Kapitza conductance, Phys. Rev. ST Accel. Beams **13**, 093503 (2010).

[50] P. Dhakal, G. Ciovati, and G. R. Myneni, Role of thermal resistance on the performance of superconducting radio frequency cavities, Phys. Rev. Accel. Beams **20**, 032003 (2017).

[51] S. W. V. Sciver, *Helium Cryogenics*, International Cryogenics Monograph Series 2nd ed. (Springer, Boston, MA, 2012).

[52] S. Inui, M. Hulse, T. Kanai, and W. Guo, Boiling peak heat flux for steady inhomogeneous heat transfer in superfluid ^{4}He, Phys. Rev. B **108**, 174509 (2023).

[53] M. W. McGee, E. R. Harms, A. L. Klebaner, J. R. Leibfritz, A. Martinez, Y. M. Pischalnikov, and W. Schappert, Investigation of thermal acoustic effects on SRF cavities within CM1 at Fermilab, in *Proceedings of International Particle Accelerator Conference, IPAC 2016* (JACoW, Geneva, Switzerland, 2016), WEPMR005.

[54] S. Barbanotti (private communication).